Research Article

SOHAG JOURNAL OF SCIENCES

https://doi.org/10.21608/sjsci.2025.330130.1230

Aeromagnetic Studies on the Great Sand Sea Area, Western Desert, Egypt

Abdelabaset M. Abudeif [1,*], Mahmoud M. Senosy[2], Farouk A. Mahmoud[1], and Mennatullah A. Shalkamy[1]

[1] *Geology Departement, Faculty of Science, Sohag University, Sohag 82524, Egypt.*
[2] *Geology Departement, Faculty of Science, Assuit University, Assuit, Egypt.*
[*]*Email: a.abudeif @science.sohag.edu.eg*

Received: 30th October 2024, **Revised:** 24th November 2024, **Accepted:** 1st January 2025
Published online: 28th February 2025

Abstract: This study evaluates the basement depth and identifies contact zones of magnetic source bodies in the Great Sand Sea, Western Desert, Egypt, using aeromagnetic data. A reduced-to-pole (RTP) aeromagnetic map reveals anomalies of varying frequency, trends, and magnitudes linked to diverse subsurface sources. Advanced processing techniques, including fast Fourier transform, distinguish residual from regional components and provide a radially averaged power spectrum, identifying three depth components: crustal thickness (~25.8 km), deep sources (~7.8 km), and shallow sources (~3.4 km). Edge detection methods, such as tilt angle and horizontal gradient derivatives, delineate structural frameworks consistent across analyses. Depth to the basement surface, determined through analytical signal and source parameter imaging, ranges from 1 km to 8.5 km. Globally, this research contributes to understanding regional tectonic settings and crustal structures, offering insights into hydrocarbon exploration and geothermal energy potential in similar arid environments worldwide.
Keywords: Aeromagnetic data, Western Desert, Great Sand Sea, Basement structure.

1. Introduction

The research area is situated in the middle part of the Egyptian Western Desert. Latitudes 25° to 29° N and longitudes 25° to 29° E form its boundaries Fig 1 Our study area is 160,000 km^2 in total. It contains several geomorphological landforms such as the Great Sand Sea (GSS) and the surrounding oases that are located within the study area. The Great Sand Sea remains a remote and largely unexplored region that fascinates the geophysicists to do studies in order to get information about the geological and structural setting of this promising area. The Great Sand Sea is really not limited to Egypt alone; it also stretches westward into Libya. It is the 15th biggest sand sea worldwide and the 7th largest in Africa [1]. With an area of around 114,000 km^2, it stretches approximately 600 km from the southern borders of the Siwa Depression in the north to the northern edges of the Gilf Kebir in the south. Its width varies between 60 and 200 km from east to west [2]. The Farafra Oasis at the west of the study area is considered one of the largest tectonic depressions situated within the Egyptian Western Desert that originated on the limestone plateau with irregular triangle and apexes heading towards Dakhla Oasis [3]. Baharia Oasis which is a large oval shaped depression that is oriented in a NE-SW direction [4] at the northwest part of the study area, and part of Dakhla Oasis at the southwest side which is one of the most historically rich and geographically diverse oases in Egypt [4]. The most challenging aspect of interpreting magnetic data is understanding its geological significance using the corrected and reprocessed magnetic measurements [5]. So, two factors can complicate the interpretation of magnetic data [6]: the di-polarity of the magnetic field, and the extra unidentified elements caused by the rocks' magnetisation direction. Despite these complexities, when used for the right kind of problem, magnetic surveys and their good interpretations can yield extremely valuable geological information [5]. Many authers have used aeromagnetic data to delineate the main tectonic trends in selected sites of the western desert [3, 4, 7– 9]. The potential field data has been used in an area that is located in the central part of the Western Desert in Egypt to determine the structures in the area and their relation to basin structure [10]. Aeromagnetic data are used to evaluate the features of subsurface structures at Farafra Oasis, Western Desert of Egypt [3]. Magnetic and gravity data are used to clarify the structural framework driving sedimentary basins in the east of the Qattara Depression area, Egypt [11]. An integrated interpretation of gravity and magnetic anomaly maps is used to analyse sedimentary cover thickness and structural patterns in the northwestern area of the Western Desert in Egypt. [12]. The present study aims to use aeromgnaetic data that obtained from the Egyptian General Petroleum Corporation (EGPC) to delineate the basement surface and detect the sedimentary cover thickness in addition to determine the tectonic framwork and subsurface structures within the studied region.

2. Geological Setting

The geological setting and sedimentary sequence of the western desert is described recently by [13, 14].

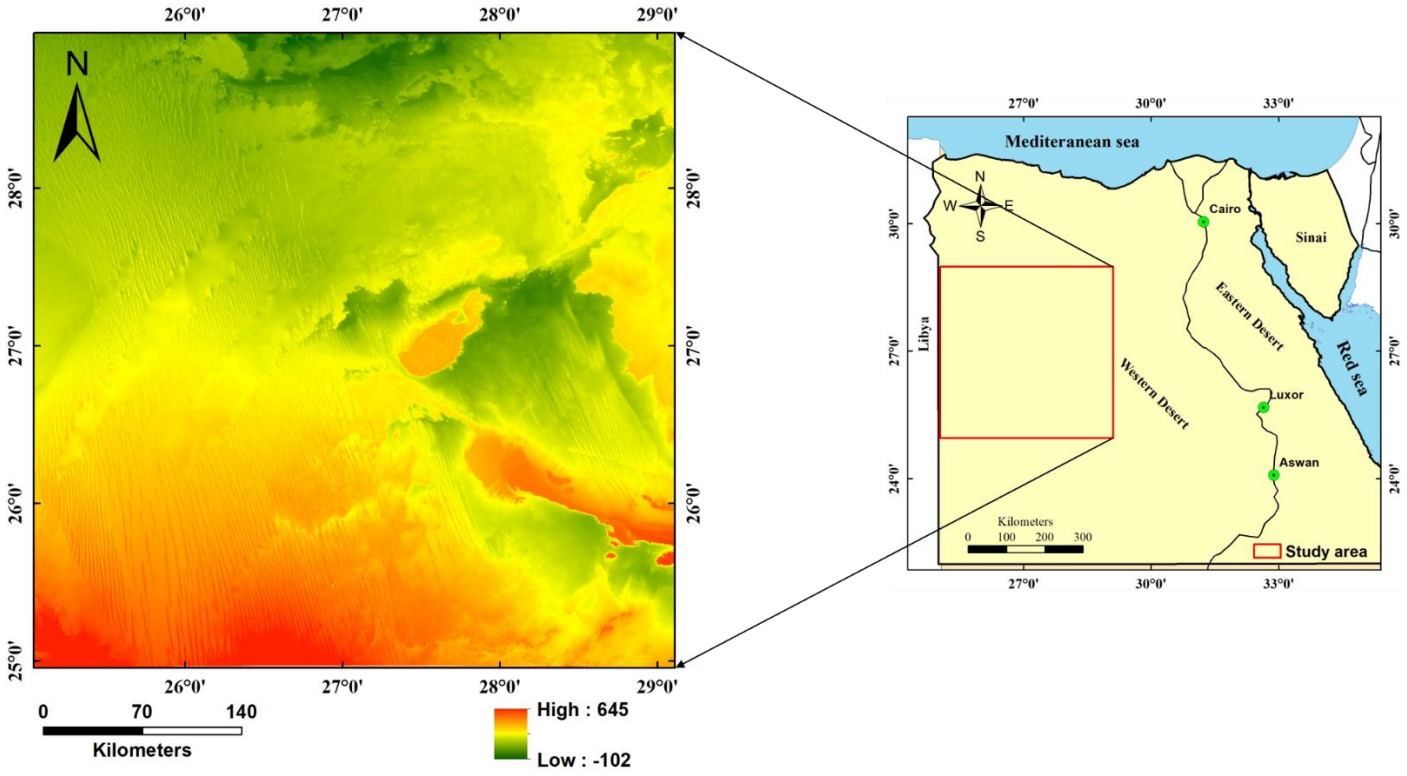

Figure 1: Location and topographic map (DEM from a satellite dataset) of the study area

Geomorphologically, Great Sand Sea is a large basin that spans from Siwa Depression in the north to Gilf Kebir Plateau in the south. It is dominated by various types of dunes, including longitudinal dunes (seif dunes), transverse dunes, and star dunes [2]. The geological map of the study area was traced from the geological map of Egypt prepared by [15] using CorelDraw ver.17 (Fig. 2). The lithostratigraphic sequences of the Western Desert from Pre-Cambrian to Recent can be described as follows (Fig. 3).

2.1. The Paleozoic successions

Thick tectono-stratigraphic layers of fluviatile to shallow-marine sediments were deposited above the Precambrian basement rocks throughout the Late Proterozoic and Paleozoic periods, creating depo-centers associated with a variety of orogenic occurrences. According to [16] these Paleozoic facies are described from base to top as follows:

2.1.1 Shifa Formation (Late Cambrian – Early Ordovician, 300-1500 m):

It is made up of a variety of sandstones, incorporating claystone, conglomerate, and frequently dolomitised skeletal carbonate.

2.1.2 Kohla Formation (Early to Middle Silurian, 80 – 600 m):

This formation is composed of fluvioglacial sandstone and mudstone sediments. [17].

2.1.3 Basur Formation (Late Silurian, 400 – 700 m):

It contains sandstone, little interbedded siltstone, and conglomerate. Alluvial fan and braided stream deposits are recorded.

2.1.4 Zeitoun Formation (Devonian, 900-1200 m):

It composed of shallow-marine sandstone and offshore marine mudstone with little conglomerate become more abundant toward the top. Limestone bands are common in the lower part.

2.1.5 Desouqy Formation (Tournaisian - Early Visean, 100 – 300 m):

This formation consists of bedded sandstone with minor intercalated carbonaceous siltstone and mudstones. More marine beds were recorded in the west whereas more continental facies were deposited southward.

2.1.6 Dahiffan Formation (Late Visean - Early Namurian, 300 m):

It consists of sandstone, mudstone, calcareous and carbonaceous, with oolitic and skeletal limestone.

2.1.7 Safi Formation (Permian, 300-400 m):

It consists of regressive sandstone and siltstone with fluviodeltaic mudstone and marine offshore oolitic limestone.

2.2. Mesozoic successions

Triassic sediments were not recorded in GSS. Jurassic continental and marine sediments and Cretaceous marine sediments represent the most Mesozoic facies in the study area. According to [18], these formations are described as follows: -

2.2.1 Bahrein Formation (Early Middle Jurassic, 300-500 m):

It consists of fine to coarse sandstones of reddish colour with thin pebbles interbeds, siltstones, and shales that are occasionally carbonaceous or pyritic. A few anhydrite bands were found in particular wells.

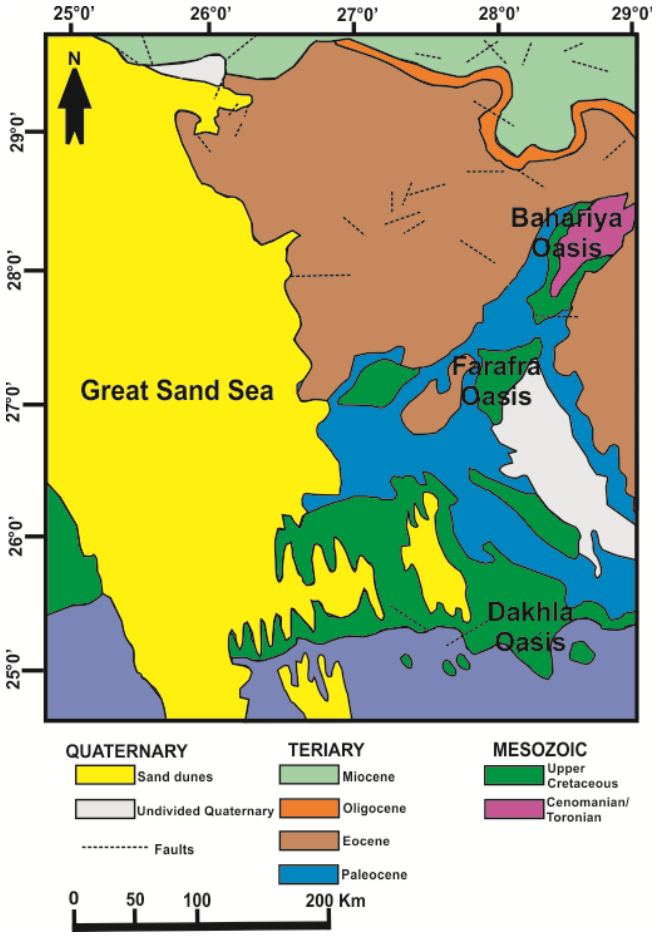

Figure 2: Geological map of the study area, middle Western Desert, Egypt, modified after [15].

2.2.2 Wadi Natrun Formation (Early Middle Jurassic, 500 m):

This formation consists of marine carbonate-shale sequence. The formation was formed in a shallow marine low energy environment, according to the paleontological and sedimentological data.

2.2.3 Khatatba Formation (Middle Jurassic, 1200 to 1400 m):

It consists of a few interbeds of limestone among the massive alternations of sandstones and shales.

2.2.4 Masajid Formation (Middle-Late Jurassic):

It assumes 450 m thick reefal facies of dolomitic limestone that transition to marl and ultimately shale layers. Chert bands intercalated with the carbonates. Shallow marine deposits that were formed in an environment with comparatively little energy make up this formation. Dolomite with shale interbeds transitioning lower to alternations of sandy to silty limestone, brown calcareous shales, and white calcareous sandstone [19].

2.2.5 Burg El Arab Formation (Neocomian-Early Cenomanian, 500-2000 m):

It is made up of clastic with fine to coarse grains. The formation is divided into four units; the Alam El Bueb sandstone, Alamein Dolomite, Dahab shale and Kharita sandstone members [19].

2.2.6 Bahariya Formation (Cenomanian, 50-1800 m):

In the drill holes in the northwestern Desert, the lithology of this formation resembles to the outcropping sediments in the Bahariya Oasis. These sediments are sandstone, siltstone, clay and a limestone [20].

2.2.7 Abu Roash Formation (Cenomanian - Turonian - Santonian, 250-1920 m):

It consists mainly of limestone sequence with shale and sandstone interbeds.

2.2.8 Khoman Formation (Maastrichtian, 100-1650 m):

The Khoman is a unique white chalk and chalky limestone with many chert bands and thin shale strata at the base. This formation was formed in an open marine, outer shelf environment.

2.3. Cenozoic successions

The Cenozoic basin was filled with mixed carbonates and siliciclastic deposits from the Oligocene, Eocene, and Miocene epochs. Cycles of transgressions and modest regressions form sedimentary successions, which yield deposits of marine, transitional, and continental deposition [21].

2.3.1 Apollonia Formation (Paleocene-Middle Eocene, 250 m):

The Eocene rocks were named Apollonia Formation by oil geologists, which is a grey nummulitic limestone beds with subordinate shale members [18, 22].

2.3.2 Daba'a Formation (Upper Eocene- Oligocene, 200-830 m):

This formation was described under the Oligocene System [23] which refers to the uncovered pliocene pink limestone of the Mediterranean shore [24].

2.3.3 Moghra Formation (Early Miocene):

It is a clastic fluvio-marine delta-front succession of calcareous shale, siltstone, and sandstone that contains silicified tree trunks and vertebrate remains. In the subsurface, this widely dispersed block contains further strata of anhydrite and shale.

2.3.4 Mamura Formation (Early Miocene, 114-950 m):

This formation is the marine equivalent of Moghra Formation. It is a limestone and calcareous shale sequence [25].

2.3.5 Marmarica Formation (Middle Miocene):

The Marmarica is a series of limestone, dolomite, and shale that has rich neritic and reefal assemblages along with many oyster banks [20]. This formation extends throughout the

Marmarica plateau of the Northwestern Desert. The research area lies on both the stable and unstable shelf. The sedimentary cover of the Western Desert contains part of the foreland deposits that is the northern continental margin of the Afro-Arabic shield from the Western Desert's southernmost segment. [9]. The structural framework of Egypt can be explained using plate tectonics. The concept of plate tectonics, with respect to ocean basins and its effects of seafloor spreading, plays an important role in comprehending global tectonics. Since that the NW to WNW, NE to ENE, and E-W tectonic patterns are generally the most prominent and often seen in northern Egypt, it is reasonable to assume that these trends are the fundamental ones influencing the unstable region of the Western Desert [26].

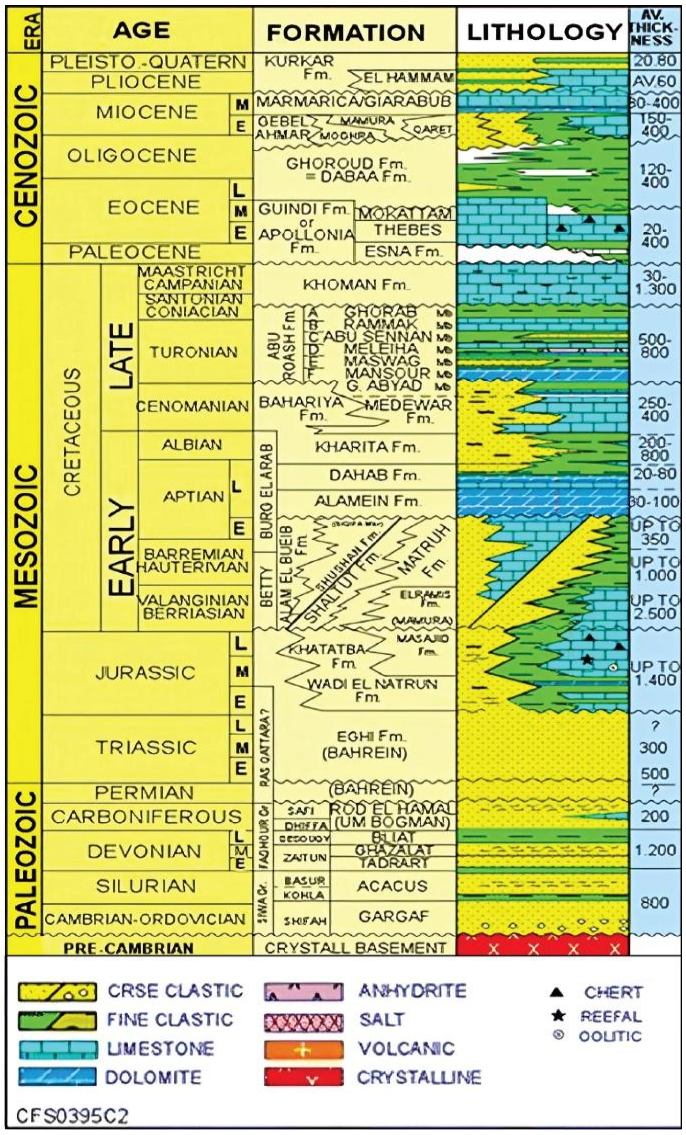

Figure 3: Lithostratigraphic column of western desert of Egypt [27].

3. Source of magnetic data

As part of the Mineral, Petroleum and Groundwater Assessment Program agreement number 263-0105, 28 September 1980 of the United States Agency for International Development, ABRO SERVICE DIVISION, WESTERN ATLAS INTERNATIONAL, INC., Houston, Texas, prepared the used magnetic data from data collected for the Egyptian General Petroleum Corporation (EGPC). Following a recompilation of previous aeromagnetic surveys across the Western Desert, more data was contributed under modification No. 1 to this agreement. The original map scale is 1:500,000 and contour interval 25 nT. The original altitude – the elevation of the sensor at the aircraft above mean sea level – was 400 feet. The total magnetic intensity of the studied area was 41,765 nT in 1989, and the magnetic inclination was 40.5°N and declination was 2.0°E; these values were used to reduce the total magnetic data to the north pole giving the RTP anomaly map. This map was digitized using Golden Surfer Sofware ver. 12 to get the RTP values at the studied site. Then, the authers used the pakage of Geosoft Oasis Montaj. Software ver. 4.8 to redraw the RTP grid and execute the processing steps to the data. These processing steps can be summarized as follow: regional/residual separation, tilt- angle derivatives, horizontal gradient, and source edge detection methods. Three techniques were used to get the depth to basement surface; the radial average power spectrum, the analytical signal and the source parameter imaging methods

4. Methodology

4.1. Regional and Residual seperation.

Spectral analysis, which theoretically depends on a fast Fourier transform (FFT), is a technique for separating regional and residual components from aeromagnetic data. It has been described by many authors e.g. [28–30]. We use this process to get the shallow and deep-seated anomalies at the study area. As a result of this process, a 2D radially average power spectrum was produced Fig. 5. By determining the wavenumber at which the spectrum's slope changes, the cutoff wavenumber was chosen (0.02 cycles/km).

4.2. Edge detection methods.

Three methods of determining contact locations and edges of anomalies; they are tilt angle derivatives (TDR) and its horizontal derivatives (THDR_TDR)., horizontal gradient (H-gradient) and source edge detection (SED).

4.2.1. Tilt derivative (TDR) and total horizontal derivative of tilt derivative (THDR_TDR).

Tilt angle derivative (TDR) filter was first proposed by [31] and later by [32]. It can be employed to map prospective mineral sites and subsurface basement structures. [33]. This approach does not require any prior knowledge of the source's structural index, however can estimate the horizontal location and depth of magnetic bodies. [34, 35] showed that the tilt angle value ranges between $\pm\pi/2$. TDR is known to draw significant attention due to its elementary and practical simplicity [36]. It can be decribed by Equation 1 as follows:

$$\text{TDR or } \theta = \tan^{-1}\left(\frac{\text{VDR}}{\text{THDR}}\right) \quad \ldots\ldots (1)$$

where θ is the local phase, VDR is the vertical derivative and THDR is the total horizontal derivative. The tilt derivatives show a significant variation with inclination; nonetheless, for inclinations of 0° and 90°, their zero-contour line is situated in close proximity to the model structures' margins. Negative

values are found farther away from the sources, and positive ones are right above them [36].

An edge detector is presented by [32], which is the THDR_TDR. It can be defined as the square root of the sum of the squares of the derivatives of the TDR in the x and y directions as shown in Equation 2:

$$\text{THDR\_TDR} = \sqrt{\left(\frac{\partial \text{TDR}}{\partial \text{x}}\right)^2 + \left(\frac{\partial \text{TDR}}{\partial \text{y}}\right)^2} \quad \ldots\ldots\ldots\ldots\ldots\ldots\ldots\ldots (2)$$

4.2.2. Horizontal gradient (H-gradient) method.

The horizontal gradient technique was first proposed by [37]. It is used intensively to interpret the RTP aeromagnetic data. This method is considered as the simplest technique to estimate the contact locations [7, 38]. The H-gradient technique is in many respects the easiest strategy for estimating contact positions of bodies at depths because of its minimal sensitivity to noise in the data, since it only needs computations of the first horizontal derivatives of the field [39]. The horizontal gradient magnitude (HGM) can be caculated by Equation (3):

$$\text{HGM} = \sqrt{\left(\frac{\partial \text{M}}{\partial \text{x}}\right)^2 + \left(\frac{\partial \text{M}}{\partial \text{y}}\right)^2} \quad \ldots\ldots\ldots\ldots\ldots\ldots\ldots\ldots\ldots\ldots (3)$$

; M is the magnetic field

4.2.3. Source edge detection (SED) method.

The SED method aims to enhance the edges of geological sources by identifying points where there is a maximum gradient in the data, which typically corresponds to the boundaries of anomalies. By analysing the local gradients, the SED can detect peaks and edges (geologic contacts) from prospective aeromagnetic data [40]. The SED locates the sudden horizontal changes in rock densities or upper crustal magnetizations by pinpointing maxima on a grid of H-gradient, TDR, and HD-TDR [41]. It is often used in conjunction with the horizontal gradient method but is optimized for pinpointing the exact edges rather than just highlighting high-gradient zones.

4.3. Estimation the depth to the basement complex.

4.3.1. Analytic signal depth technique.

This approach, which also called the total gradient method, is extremely effective in determining the margins of magnetic source bodies using Geosoft Osis Montaj Softwere ver. 8.4 [33]. According to [37–39], The analytic signal technique assumed that the sources were isolated, dipping contacts separating thick geologic sections. Analytic signal magnitude is defined as the square root of the sum of the squares of the magnetic field's vertical and horizontal derivatives [43] as shown in Equation (4):

$$AS = \sqrt{\left(\frac{\partial f}{\partial x}\right)^2 + \left(\frac{\partial f}{\partial y}\right)^2 + \left(\frac{\partial f}{\partial z}\right)^2} \quad \ldots\ldots\ldots\ldots\ldots\ldots\ldots\ldots (4)$$

The independence of inclination in identifying magnetic parameters from magnetic anomalies is one benefit of applying the AS approach. With only a few assumptions regarding the nature of the source body, typically considered to be a 2D magnetic source, the AS approach is successful in locating and estimating the depth of magnetic sources (for example, step, contact, horizontal cylinder or dike). In these geological models, the amplitude of the AS is a bell-like symmetric function positioned precisely above the source body.

The analytical signal of the first vertical derivative (AS1) can be deduced from Equation (5).

$$\text{AS1} = \sqrt{\left(\frac{\partial \text{FVD}}{\partial \text{x}}\right)^2 + \left(\frac{\partial \text{FVD}}{\partial \text{y}}\right)^2 + \left(\frac{\partial \text{FVD}}{\partial \text{z}}\right)^2} \quad \ldots\ldots\ldots\ldots (5)$$

where: the FVD is the first vertical derivative of the RTP.

So, to calculate the depth to magnetic source Equation (6) is used:

$$\text{D} = \frac{\text{AS}}{\text{As1}} * \text{N} \ldots\ldots\ldots\ldots\ldots\ldots\ldots\ldots\ldots\ldots\ldots\ldots\ldots\ldots (6)$$

where:

D is the depth of the magnetic sources, and N is a structural index that corresponds to the magnetic source's shape. For example, N = 1 for magnetic contact, N = 2 for thin dike, N = 3 for pipe and N = 4 for sphere [44].

4.3.2. Source parameter imaging (SPI) technique.

SPI, also known as local wavenumber, is an approach for estimating magnetic depths which utilizes the extension of complicated analytical signals [45]. In this technique, the function of the local wavenumber can be provided by Equation (7):

$$\text{k} = \frac{\frac{\partial^2 \text{f}}{\partial \text{x}\,\partial \text{z}}\frac{\partial \text{f}}{\partial \text{x}} - \frac{\partial^2 \text{f}}{\partial \text{x}^2}\frac{\partial \text{f}}{\partial \text{z}}}{\left(\frac{\partial \text{f}}{\partial \text{x}}\right)^2 + \left(\frac{\partial \text{f}}{\partial \text{z}}\right)^2} \quad \ldots\ldots\ldots\ldots\ldots\ldots\ldots\ldots\ldots\ldots\ldots\ldots (7)$$

Regardless of the magnetic inclination, declination, dip, strike, and any residual magnetization, for the dipping contact, maxima of k are situated directly above the isolated contact edges [45]. The depth can be calculated from Equation (8) at the source edge that derived from the local wavenumber reciprocal:

$$\text{Depth}_{(\text{x}=0)} = \frac{1}{\text{k}_{max}} \quad \ldots\ldots\ldots\ldots\ldots\ldots\ldots\ldots\ldots\ldots\ldots\ldots (8)$$

Where:

k_{max} is the maximum value of the local number k over the step source.

It is possible to determine depths without making any assumptions about the thickness of the source bodies since the local wavenumber has maxima over isolated contacts [46].

SPI method was compared with the analytic signal method by [39], and showed how the two approaches can differ in their assumptions, precision, noise sensitivity and anomaly interaction.

4.4. Subsurface trends

The center for exploration targeting (CET) grid analysis approach was used to evaluate the research area's structural

lineaments from the RTP. These structural frameworks are statistically evaluated and presented as rose diagram using Rockware ver.15 software. The azimuth and length of the identified trends are determined and statistically evaluated to determine their length and number percentages (L% and N%), as well as the number to length ratios. The principle tectonic patterns influencing the studied area were revealed by tracing and statistically analysing the magnetic lineaments in terms of number (N), length (L), L/N ratios, and direction.

The outcomes of the statistical trend analysis (L%, N%, and L/N ratio) assist in determining the number of fractures with a specific cumulative length within various locations in the study region and indicate the prevailing orientations [47].

5. Results and Discussion:

5.1. Reduced to the magnetic pole (RTP) map.

RTP is a transformation that aims to make it easier to comprehend magnetic data, independent of the source magnetization. As a result, it becomes simpler to tie the magnetic anomalies to their sources, enabling interpretation easier and more trustworthy [9]. The RTP aeromagnetic map (Fig. 4) shows values of magnetic intensity that range from -95.8 nT to +223.0 nT. This map reveals some large magnetic bands distributed over the map, which can be defined as follows: There are two large high positive anomalies (more than +170 nT) with magnita colour, one of them occur at the middle of the map to the west and other to the north which have trends in N-S, NW-SE and NE-SW directions. Furthermore, there are some small positive anomalies scatterd in the western part of the map with orientation in NE-SW and E-W. Also, there are some negative anomalies (blue colour) mainly concentrated at middle, eastern and southern parts of the studied region taking trends in N-S, E-W, NE-SW directions.

5.2. Regional–residual separation.

5.2.1. The 2D radially averaged power spectrum.

As was mentioned before, the RTP aeromagnetic survey data was subjected to the fast Fourier transformation (FFT) in order to compute the energy spectrum and get the 2D power spectrum. Based on the variation in the slope of the spectrum curve, the curve is subdivided into segments; The average depths to magnetic sources can be estimated from the slopes of these segments. The depth of each source which is responsible for each segment can be calculated by Equation (9).

$$\text{Depth} = \frac{-\text{slope}}{4\pi} \ldots\ldots\ldots\ldots\ldots\ldots\ldots\ldots\ldots\ldots\ldots\ldots\ldots\ldots(9)$$

The spectrum curve (Fig. 5) consists mainly of three segments; the first one at a low wavenumber range from 0 km^{-1} to 0.01 km^{-1} (red segment). This segment's slope denotes the highest depth which equals 25.8 Km which may reflect the crustal thickness (Curie point) at the study area. These results are compatible with several studies [48–51]. The second segment in blue colour which also at a low wavenumber from 0.01 km^{-1} to 0.1 km^{-1}, represents according to its slope the depth of deep magnetic causative bodies which may reflect the maximum depth to basement surface at 7.8 km. The third one (green colour) which is gentle in its slope at relatively high wavenumber (0.1 km^{-1} to 0.2 km^{-1}). This slope represents the shallow magnetic sources at 3.4 km which may reflect the near-surface geological structures or the minimum depth to the basement complex. The wavenumber more than 0.2 km^{-1} reflects the noise.

5.2.2. The regional magnetic map.

The low-pass map (Fig. 6) displays the high amplitude magnetic anomalies in deep depths. The magnetic intensity values of this map range from -82.2 nT to 208.6 nT.

By comparing this map with the RTP map, we can notice that the same anomalies appear in the two maps but in smoothy mannar at regional map. The same trends of the anomalies in E-W, N-S, NW-SE and NE-SW directions in ellipsoidal to elongated shape are found in this map. Negative anomalies may be defined as thick sedimentary cover enclosed within the fault-bounded borders and displaying isolated basinal structures.

Figure 4: Reduced to the magnetic pole (RTP) map of the studied area

5.2.3. The residual magnetic map.

The high-pass map (Fig. 7) enhances the effects of the shallow sources. This map consists of magnetic anomalies ranging from -60 reaching to +50 nT. The positive and negative anomalies are distributed alternately through the studied area. The trends of these anomalies are in E-W, N-S, NW-SE and NE-SW directions which are parallel to the direction of the geological and structural trends of the area. These small, circular, oval and elongated anomalies (negative and positive) show local basins and uplifts.

5.3. Edge detection methods.

5.3.1. The tilt derivative (TDR) and its total horizontal derivative (THDR_TDR) maps.

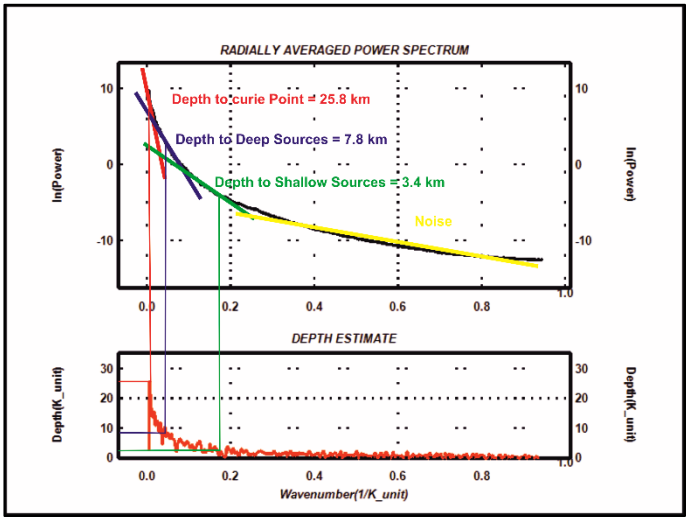

Figure 5: The radial average power spectrum (RAPS) of the study area showing average depths to curie point deep and shallow sources.

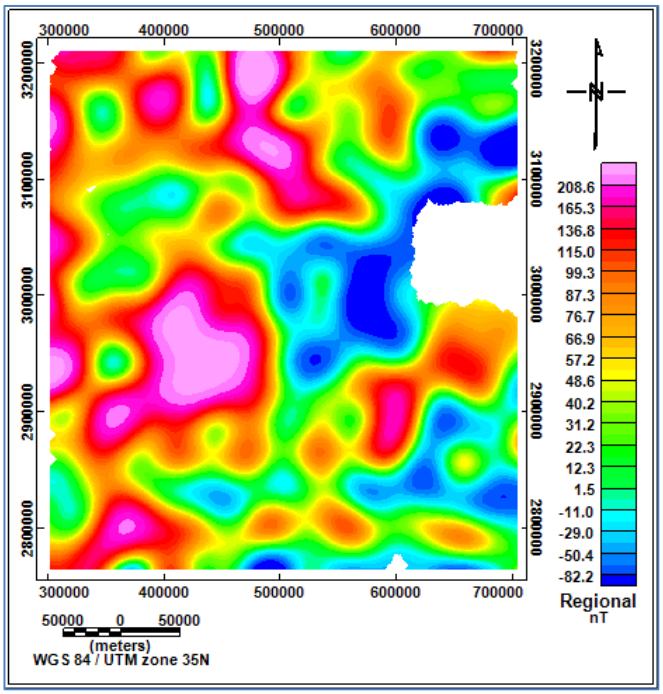

Figure 6: Low-pass (Regional) magnetic map showing deep anomalies of the studied area

According to [31], geologic structures such as faults, which can be represented as magnetic lineaments, can be obtained through the TDR analysis. The TDR map (Fig. 8) shows values range from -1.42 to 1.24 radians. The black line represents zero-contour line in the TDR map is the contact boundary of magnetic sources as it suggests the location of sudden changes of magnetic susceptibilities between negative and positive anomalies that is especially at the sharp gradient. The TDR map confirms the feature's trends at the studied area in the NW-SE, N-S, E-W and NE-SW directions.

It is showed by [53] that the boundaries of distinct peaks are specified by the THDR_TDR, which maintains amplitude improvement. Consequently, the reciprocal of the depth to the top of the magnetic source is equal to the amplitude of the THDR_TDR. According to [35], half-distance between ± 45° radians (±π/4) contours provide a determination of the depth to sources for vertical contacts. The THDR of the TDR is shown in (Fig. 9) and from the inspection of this map, we can deduce that the depth to sources range from 1.8 km up to 25 km.

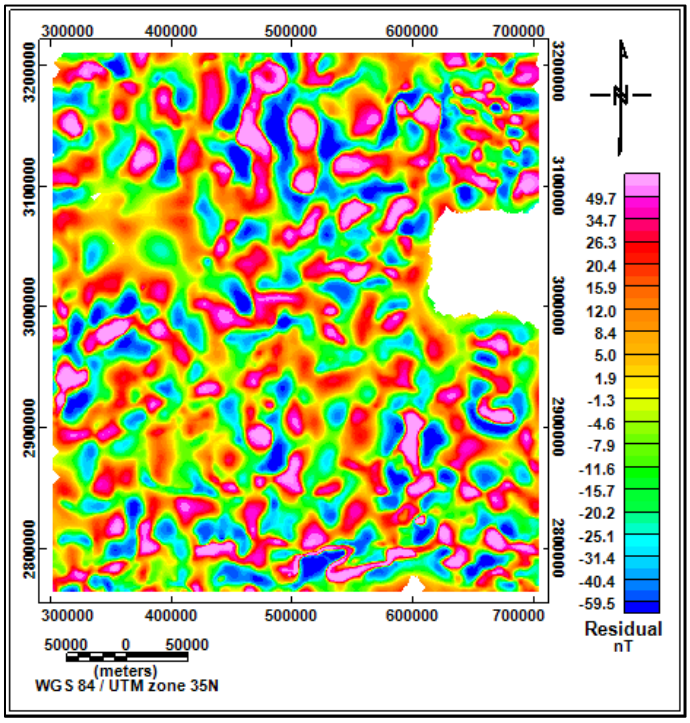

Figure 7: High pass (residual) magnetic map showing shallow anomalies of the studied area

5.3.2. The Horizontal gradient (H-gradient) map.

The H- gradient map (Fig. 10) of magnetic data refers to the pace of the changes of the strength of the magnetic field in the horizontal direction. Major tectonic trends in this map are in N-S and E-W directions with minor trends in NW-SE and NE-SW directions.

5.3.3. The source edge detection (SED) map.

The SED solutions map (Fig. 11) is utilized to detect and outline the magnetic bodies' edges. These edges correspond to geological features such as faults, intrusions, or contacts between different rock types, which exhibit a magnetic contrast. This map here refers to the source boundaries in vector format that mean it can be used to define its strike and dip. The symbols are matched with the outlines of the anomalies (Fig. 12) and the direction of the gradient also is coincident with those of the anomalies which facilities the interpretation and the analysis about the shape and distribution of anomalies in the studied area.

5.4. Basement depth estimation.

5.4.1 The analytic signal depth map.

The analytical signal approach was used in the research region to determine the depth to basement surface. In order to get this map, some processing steps were applied. Firstly, AS filter was applied on RTP map to get AS map (Fig. 13) that displays the magnetic sources' edge positions in both horizontal and vertical directions. Secondly, the first vertical derivative filter was applied on the RTP data. This map (Fig. 14) shows alternatives between negative and positive anomalies which are coinsides with the TDR map (Fig. 8) in the direction and trends. The zero-contour line here also determines the contact between negative and positive anomalies. Thirdly, the AS also was applied on FVD map to get the AS of FVD map (Fig. 15). According to Equation (6), the analytical signal of reduced to pole (AS) map (Fig. 13) is divided by the analytical signal of first vertical derivate (AS1) map (Fig. 14) and multiplied by 1 to get the depth to basement surface of the study area (Fig. 16). This map shows depths range from -1064 m to -8498 m. The shallow depths of the studied area may be correlated to the uplifts due to strctures, volcanic intrusions and/or dikes, while the deep depths can be attributed to some thick sedimentary cover.

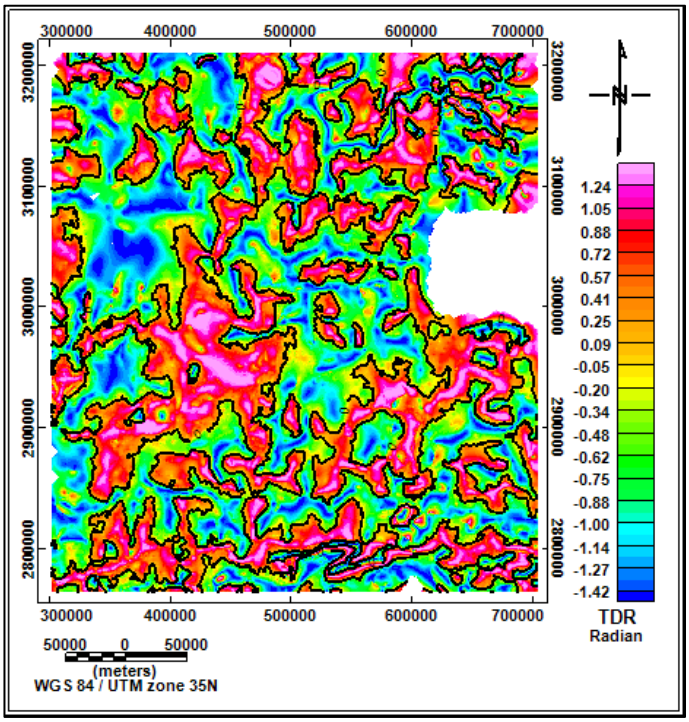

Figure 8: Tilt angle derivative (TDR) map of the studied area with zero contour line.

5.4.2. The source parameter imaging (SPI) map.

The SPI map (Fig. 17) shows a good similarity in depth estimation to the basement relief using the AS depth map (Fig. 16). Here the depth to basement complex ranges between -1139 m to -8045 m. These results are matched with results of [3] specially in the western part of the study area and with [7] in northwestern part of the studied area.

5.5. Structural interpretation of the aeromagnetic data

The RTP map was used to analyze the structural lineaments in the research region (Fig. 18 **and** 19). These lineaments are studied statistically and plotted in rose diagram (Fig. 20) and have variable intensities and lengths that are shown in (Table 1).

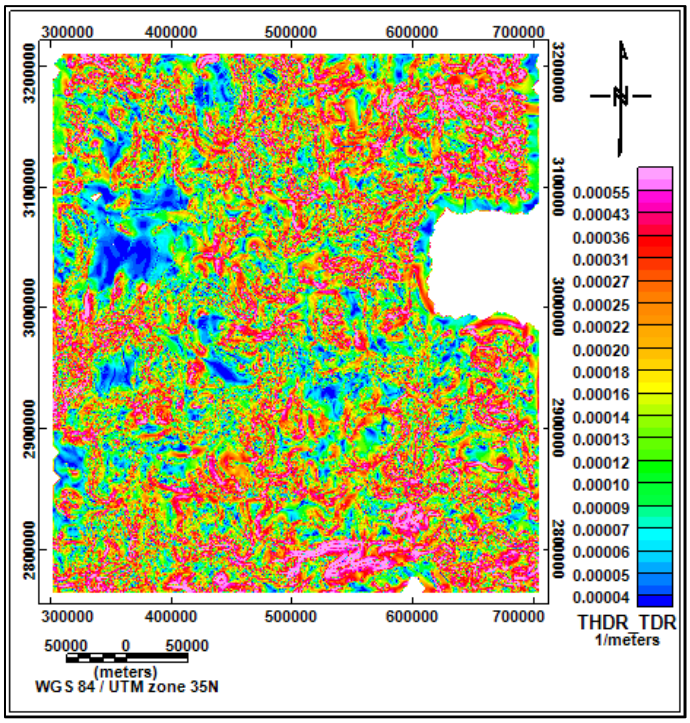

Figure 9: Total horizontal derivatives of the tilt angle derivative (THDR_TDR) map of the studied area

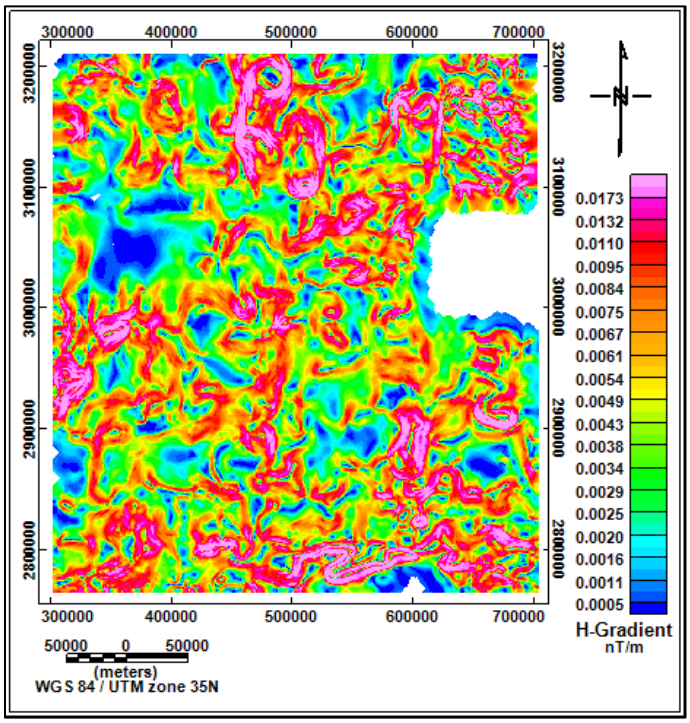

Figure 10: Horizontal gradient (H-gradient) map of the studied area

The total number of geological or structural lineaments identified in the study area is 288 with total lengths 5706.5 km. It also shows the percentage of lineament number to total number (N%) which indicates the proportion of lineaments in a specific direction relative to the total number of lineaments

across all studied areas or sectors. The table also shows percentage of lineament length to total length (L%) which

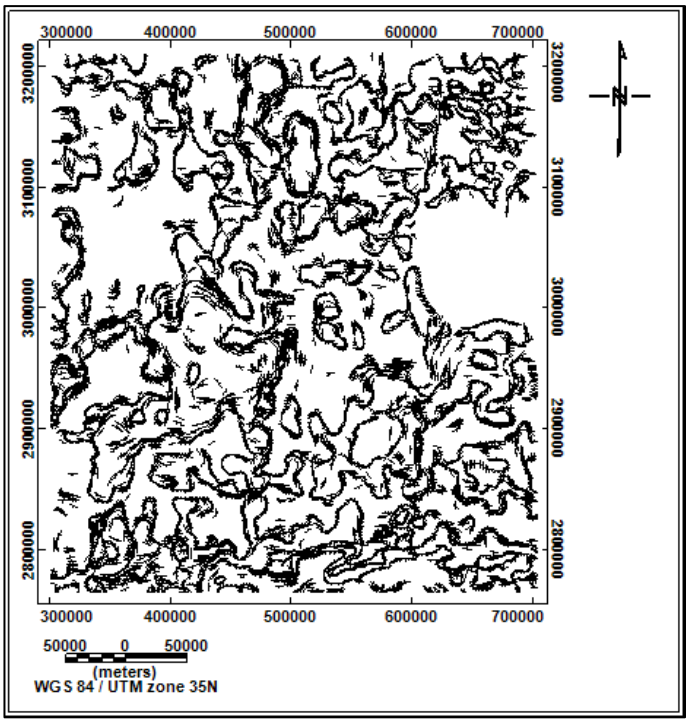

Figure 11: Source edge detection solutions (SED) delineate the boundaries of subsurface structures of the studied area

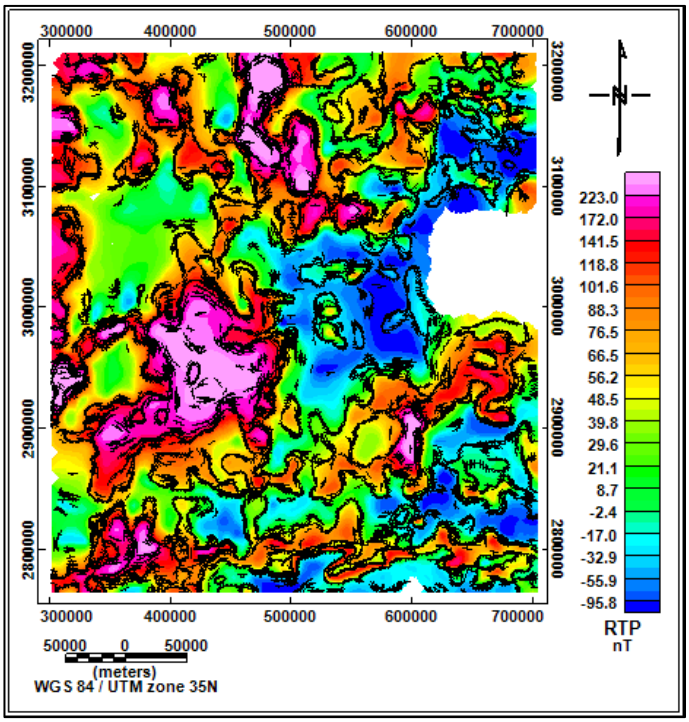

Figure 12: Source edge detection (SED) solutions plotted on the RTP map of the studied area

represents the proportion of the total length of lineaments in a specific trend relative to the total length of all lineaments in the trends. In addition to that (L/N) which represents the average length of a single lineament in a specific trend. All lengths are represented in meter. The trend analysis of this diagram reveals that the dominating lineament patterns are often E-W to ENE-WSW, with subordinate N-S to NNE-SSW trends influencing the researched region as derived from the geomagnetic viewpoint view. Other minor structural trends occur in the NE-SW and NW-SE directions. The mean direction of these lineaments in NE-SW direction which compatible with the results of [8, 11, 50, 52].

The results that obtained from our study can be sumarrizied as follows: (1) the depth to very deep sources reaching curie point is 25.8 km which matches with results of [8, 9, 51, 52] (2) the depth to basement surface ranges between 1 to 8 km with average depth 3 km along the study area; these results matches with the results of [3, 4, 7, 9] (3) the structural lineaments analysis of the study area shows that the area has several trends; the E-W to ENE-WSW trends which are generally linked to regional tectonic regimes and the influence of the Syrian Arc trend which is a prominent structural feature associated with Hercynian Orogeny and the Tethyan orogeny [7, 11, 19, 54], while the N-S to NNE-SSW trends may relate to rift-related tectonic forces, such as the Red Sea rifting [7, 19], and the NE-SW direction (aulitic trend) [3] which may be linked to younger tectonic events or fracture systems.

Table 1: Statical analysis of lineaments bearing from RTP map

No.	Azimuth	N	L	N%	L%	L/N
1	0° - < 10°	25	564430.62	8.68056	9.89101	22577.2
2	10° - < 20°	23	435202.17	7.98611	7.62643	18921.8
3	20° - < 30°	11	164097.18	3.81944	2.87562	14917.9
4	30° - < 40°	15	291673.95	5.20833	5.11126	19444.9
5	40° - < 50°	13	241675.68	4.51389	4.23509	18590.4
6	50° - < 60°	10	191754.84	3.47222	3.36029	19175.5
7	60° - < 70°	21	353406.59	7.29167	6.19305	16828.9
8	70° - < 80°	21	382203.86	7.29167	6.69769	18200.2
9	80° - < 90°	26	524816.43	9.02778	9.19682	20185.2
10	90° - < 100°	28	564707.74	9.72222	9.89587	20168.1
11	100° - < 110°	12	202233.42	4.16667	3.54391	16852.8
12	110° - < 120°	19	382591.83	6.59722	6.70449	20136.4
13	120° - < 130°	11	244750.71	3.81944	4.28898	22250.1
14	130° - < 140°	7	129664.86	2.43056	2.27223	18523.6
15	140° - < 150°	5	68646.93	1.73611	1.20296	13729.4
16	150° - < 160°	9	181556.56	3.125	3.18157	20173
17	160° - < 170°	20	381856.73	6.94444	6.69161	19092.8
18	170° - < 180°	12	401230.59	4.16667	7.03111	33435.9
Total		288	5706500.69	100	100	

N: Number of lineaments.
L: Total length of linements in meter.
N%: Percentage of lineaments number to total number.
L%: Percentage of lineaments length to the total lengths.

6. Conclusion

In the present study, the RTP aeromagnetic map was utilized to delineate the subsurface structures and depth to basement surface in the Great Sand Sea region and its surrounding areas that cover about 1/6 of Egypt total area by applying several processing techniques using Geosoft Oasis Montaj ver. 4.8. First, the Fourier transform was applied to the RTP data to get high-and low- pass maps of the research area, the cutoff

wavenumber value is 0.02 cycles/km. The results of the radial average power spectrum (RAPS) show three main segments; the deepest depth representing the curie depth point at 25.8 km then the second slope which represent the mean depth to regional components at 7.8 km and finally, the mean depth to the shallow source which reaches 3.4 km. Three edge detection processing techniques were used in this study to locate the edges of the magnetic bodies: tilt angle derivative (TDR) and its total horizontal derivative (THDR-TDR), the horizontal gradient (H-gradient) and the source edge detection (SED). These methods reflect similar results in determining magnetic contacts. The Zero contour line of the TDR map depicts these source magnetic edges. These edges seem sharper on the THDR_TDR map, whose values correspond to the reciprocal of the depth to these edges. The SED map refers to the source boundaries in vector format which matched with the H-gradient and TDR maps. The depth to basement surface was deduced using AS and SPI methods and show similar results ranging from 1 km to 8.5 km. Using a tentative structure map that was applied from the RTP map, two major structure trends are presented in the ENE-WSW and NNE-SSW directions with minor trends in the NE-SW and NW-SE directions. It is recommended to apply seismic reflection methods. This technique will provide high-resolution subsurface imaging, making it particularly valuable for hydrocarbon exploration. The detailed structural mapping obtained through seismic surveys can help identify potential traps and reservoirs, enhancing the understanding of the area's petroleum potential. Additionally, implementing electrical and electromagnetic geophysical methods is suggested for groundwater exploration. These methods are highly effective in detecting subsurface water-bearing formations and can support the sustainable development of the region. The integration of these geophysical techniques will offer a comprehensive assessment of the area's resources, serving both economic and environmental objectives.

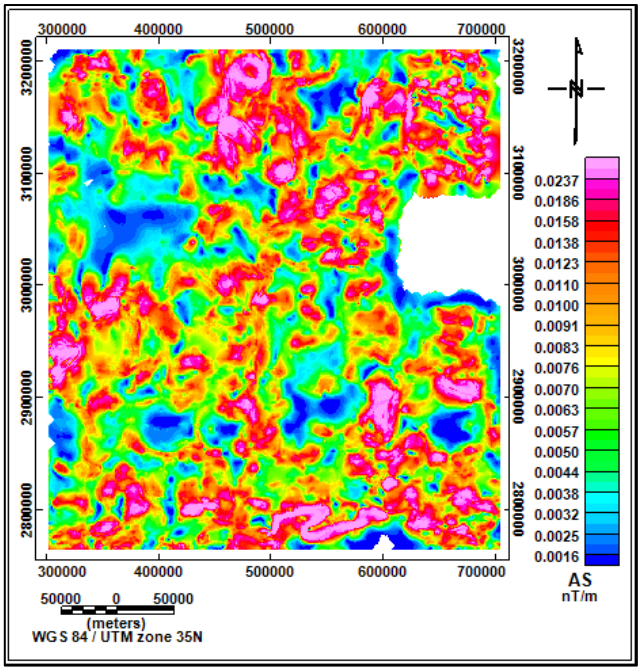

Figure 13: Analytical signal (AS) map of the studied area

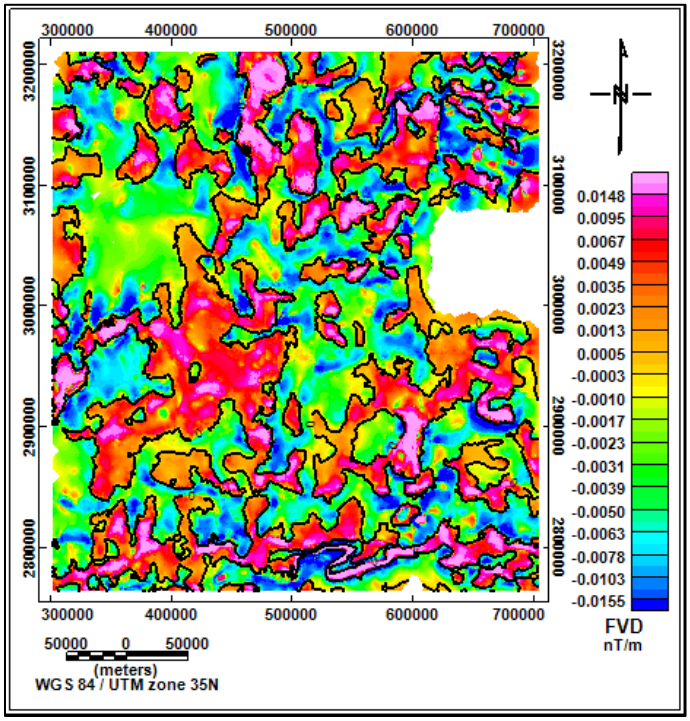

Figure 14: First vertical drevative (FVD) map of the studied area

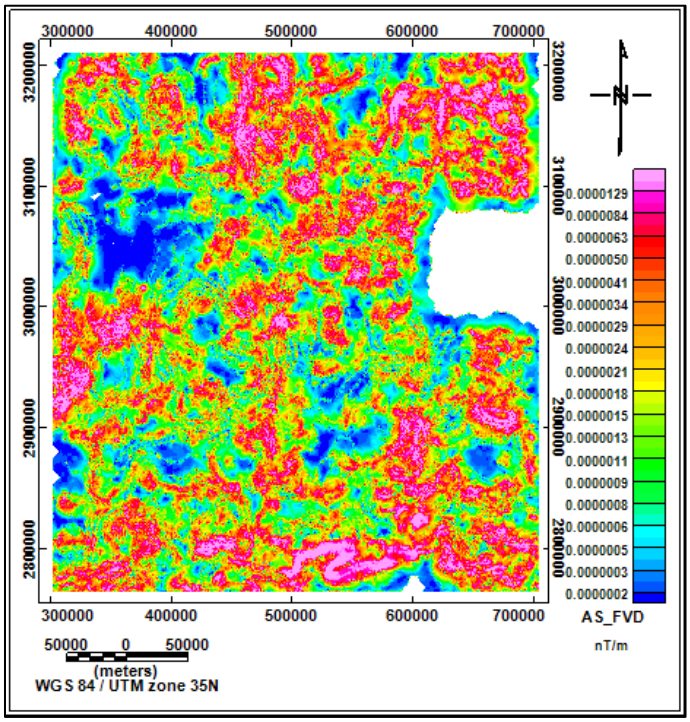

Figure 15: Analytical signal of the first vertical drevative (AS_FVD) map of the studied area

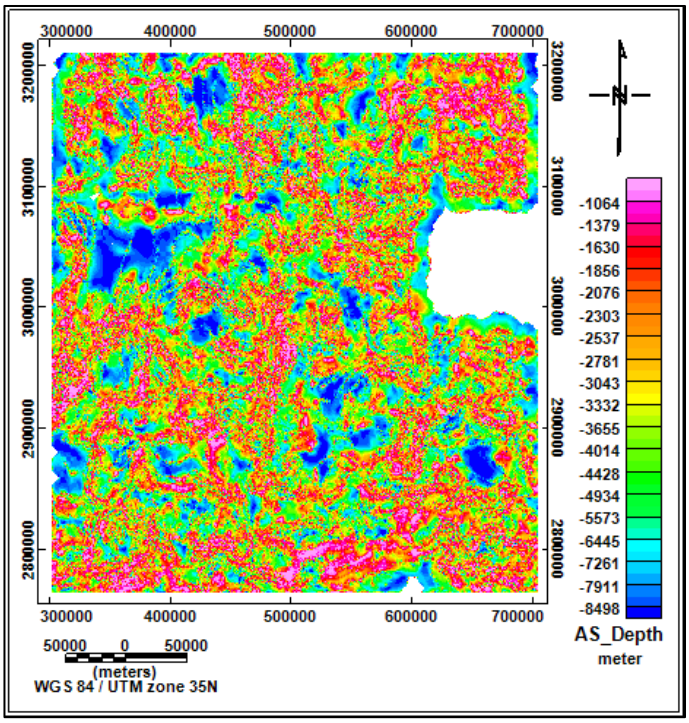

Figure 16: Analytical signal depth (AS_Depth) map showing depth to basement surface at the studied area

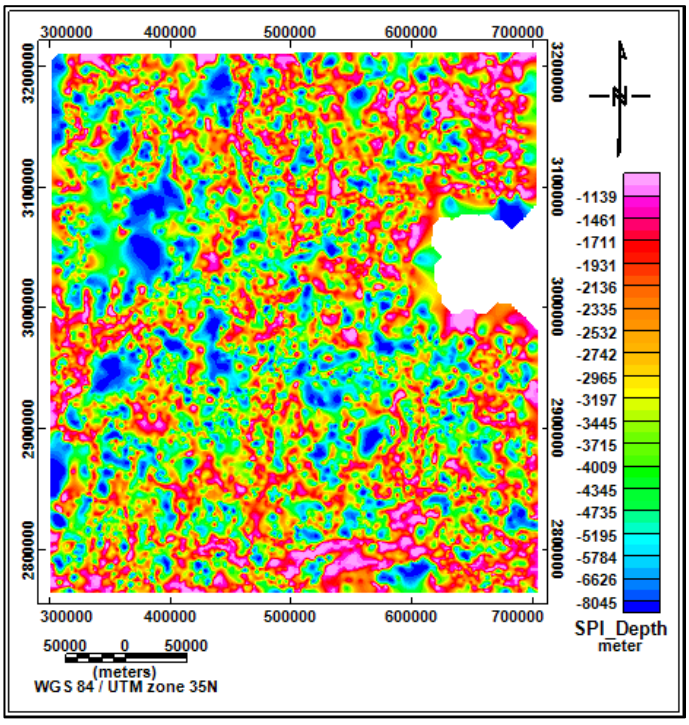

Figure 17: Source parameter imaging (SPI) map showing depth to basement surface at the studied area

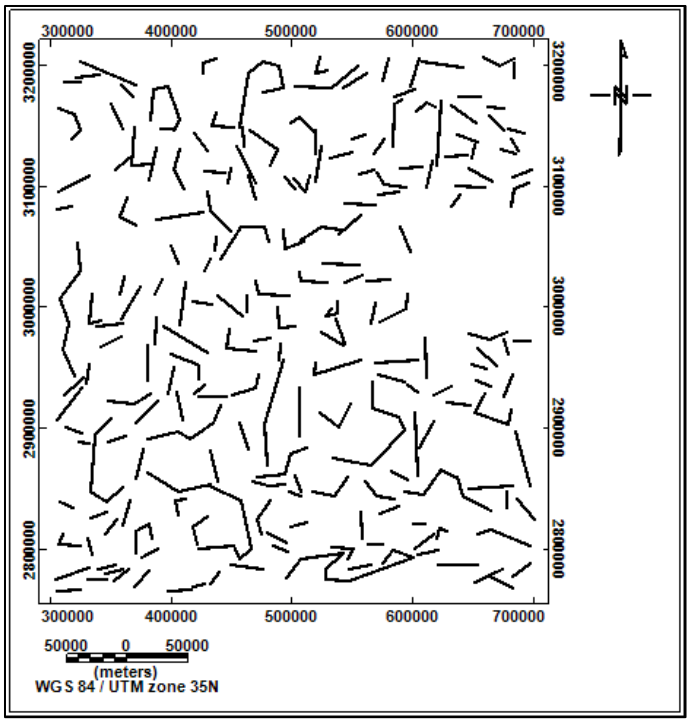

Figure 18: A tentative basement structure map of the studied area

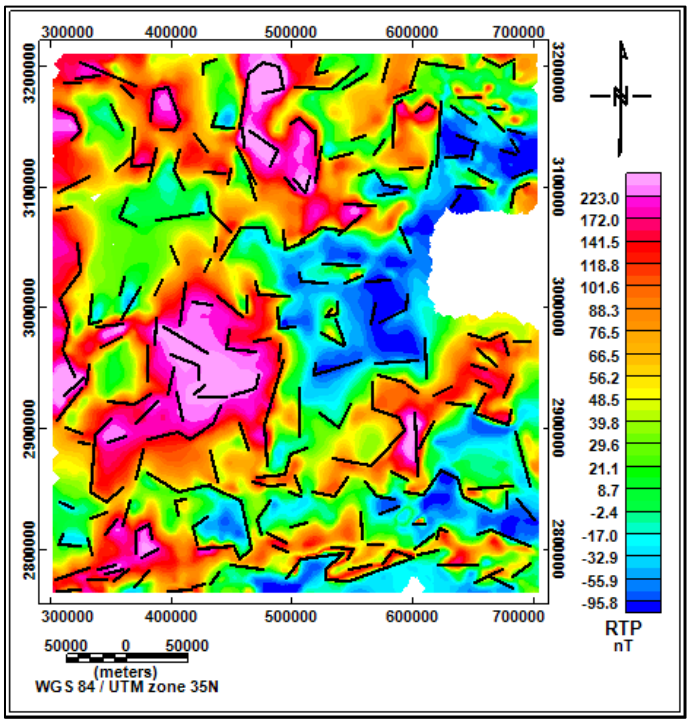

Figure 19: The structure lineaments plotted on RTP map of the studied area

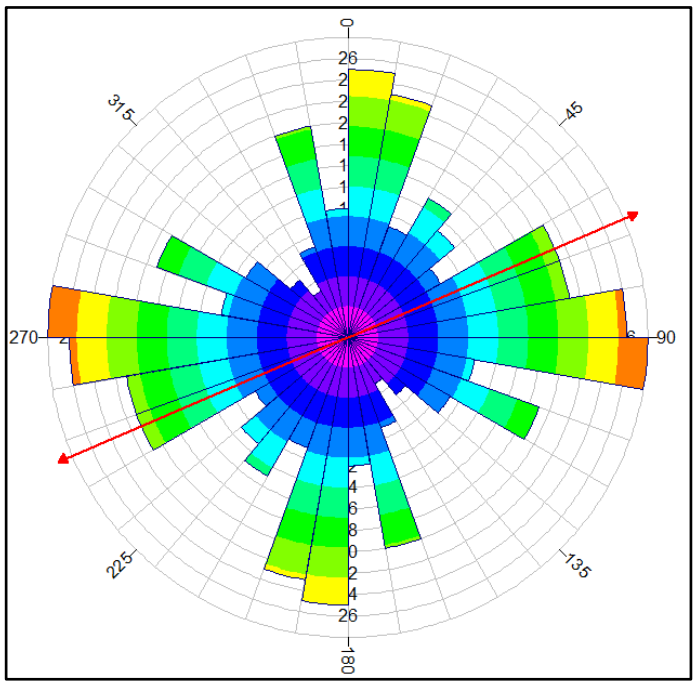

Figure 20: Frequency bearing rose diagram deduced from lineaments extracted from RTP map

CRediT authorship contribution statement:

Conceptualization, Abudeif, A.M. and Senosy, M.M.; methodology, Shalkamy, M.A.; software, Shalkamy, M.A.; validation, Abudeif, A.M., Mahmoud, F.A., and Senosy, M.M.; formal analysis, Shalkamy, M.A.; investigation, Abudeif, A.M.; resources, Senosy, M.M.; data curation, Senosy, M.M.; writing—original draft preparation, Shalkamy, M.A.; writing—review and editing, Abudeif, A.M.; visualization, Mahmoud, F.A.; supervision, Abudeif, A.M. and Mahmoud, F.A.; project administration, No.; funding acquisition, No. All authors have read and agreed to the published version of the manuscript.

Data availability statement

The data used to support the findings of this study are available from the corresponding author upon request.

Declaration of Competing Interest

The authors declare that they have no known competing financial interests or personal relationships that could have appeared to influence the work reported in this paper.

Acknowledgments

The authors would like to express their special thanks and gratitude to the Egyptian Geological Survey and Mining Authority and the Egyptian General Petroleum Corporation (EGPC) for providing us with the gravity and magnetic information used in this work.

References

[1] I.G. Wilson, *Sedimentary Geology* 10, (1973) 77–106.
[2] N.S. Embabi, Landscapes and landforms of Egypt. Springer, 2018.
[3] M.M. Khalifa, W.H. Mohamed, M.A. El Ammawy, A.I. Taha, A. Awad, and A.A. Orchid, *Modeling Earth Systems and Environment*, 10 (1), (2024) 723-733.
[4] E.A. El All, A. Khalil, T. Rabeh, and S. Osman, *NRIAG Journal of Astronomy and Geophysics*, *4*(2), (2015) 236-248.
[5] M.A. Al-Badani, and Y.M. Al-Wathaf, *Egyptian Journal of Petroleum*, 27(4), (2018), 485-495.
[6] P.V. Sharma. Geophysical Methods in Geology, Elsevier Scientific Publishing Company, Amsterdam, The Netherland, 1976.
[7] W. Araby, S.H. Abd, A.E. Aref, I. Al-Alfy, M.M. Abdullah, and A.A. Elhusseiny, *The Leading Edge*, *40*(10), (2021) 724-733.
[8] M.A. Zaher, H. Saibi, K. Mansour, A. Khalil, and M. Soliman, *Renewable and Sustainable Energy Reviews*, *82*, (2018) 3824-3832.
[9] H.S. Mohamed, M.M. Senosy, and M.A. Zaher, *Journal of Applied Geophysics*, 134, (2016) 291-302.
[10] M. Kamal, J. Shen, A.A. Othman, S.A. Araffa, H.O. Tekin, A. Ene, A.S. Abdel-latief, and H.M. Zakaly, *Open Chemistry*, *21*(1), (2023) p.20220293.
[11] S.A. Saada, A.M. Eldosouky, M. Kamel, A. El Khadragy, K. Abdelrahman, M.S. Fnais, and K.Mickus, *Journal of King Saud University-Science*, *34*(2), (2022) p.101808.
[12] A.A. El Khafeef, M.H. Saad, A.A. Azab, and S.A. Soliman, *World Appl. Sci. J*, *31*(7), (2014) 1257-1268.
[13] A.E. Radwan, *The Phanerozoic Geology and Natural Resources of Egypt*, (2023) 691-717.
[14] A.E. Radwan, The Geology of North Africa 221-249. Cham: Springer International Publishing. 2024.
[15] CONOCO and EGPC, (1987): "Geological map of Egypt. Scale 1:500 000.
[16] M.L. Keeley, *Basin Research*, *2*(1), (1989) 35-48.
[17] B.Issawi, and S. Farouk, *The Phanerozoic Geology and Natural Resources of Egypt*, (2023) 3-26.
[18] G. Hantar, In, R. Said (Ed.), The Geology of Egypt. A.A. Balkema, Rotterdam, (1990) p. 293-319.
[19] R. Said, The geology of Egypt. Balkema, Rotterdam, 734 P, 1990.
[20] R. Said, The geology of Egypt, Amsterdam-New York, Elsevier Publishing Co., 337 P, 1962.
[21] D.S. Macgregor, and R.T. Moody, *Geological Society, London, Special Publications*, *132*(1), (1998) 201-216.
[22] M.H. Elzarka, and I.A.F. Radwan, *Journal of African Earth Sciences*, 5(3), (1986) 285-319.
[23] P. Norton, report No. 4, Pan American Oil Company, Cairo, Egypt, 1967.
[24] A.M. Abdallah, *Geo. Surv.*, (1966) 45: 1.9.
[25] I. Marzouk, 7th Arab Petrol. *Congr. Kuwait*, *54*. 1969.
[26] N. Sultan, and M.A. Halim, The Egyptian General Petroleum Corporation , v. 2, (1988) 1–22.
[27] Schlumberger. Well evaluation conference, (1984) 1-64.
[28] Y. Li, and D.W. Oldenburg, *Geophysics*, *63*(2), (1998) 431-439.
[29] R.J. Blakely, *Potential theory in gravity and magnetic applications*. Cambridge university press, 1996.
[30] A. Spector, F.S. and Grant, *Geophysics*, *35*(2), (1970) 293-302.
[31] H.G. Miller, and V. Singh, *Journal of applied Geophysics*, *32*(2-3), (1994) 213-217.
[32] B. Verduzco, J.D. Fairhead, C.M. Green, and C. MacKenzie,.*The leading edge*, *23*(2), (2004) 116-119.
[33] Geosoft oasis montaj, V.8.4. Geosoft Software for the Earth Science, Geosoft Inc., Toronto, Canada, 2015.
[34] A. Salem, S. Williams, D. Fairhead, R. Smith, and D. Ravat, Geophysics, 73(1), (2008) L1-L10.
[35] A. Salem, S. Williams, J.D. Fairhead, D. Ravat, and R. Smith, *The leading edge*, *26*(12), (2007) 1502-1505.
[36] W.J. Hinze, R.R. Von Frese, R. Von Frese, and A.H. Saad, *Gravity and magnetic exploration: Principles, practices, and applications*. Cambridge University Press, 2013.

[37] W.R. Roest, J.J. Dañobeitia, J. Verhoef, and B.J. Collette, *Marine Geophysical Researches*, *14*, (1992) 1-24.
[38] G.M. Gaber, S. Saleh, and M. Toni, Acta Geophysica, 70(2), (2022) 639-657.
[39] J.D. Phillips, *SEG Technical Program Expanded Abstracts* (2000) 402-405.
[40] N. Whitehead, and C. Musselman, Montaj grav/mag interpretation. Processing, Analysis and Visualization system for 3D Inversion of Potential Field Data for Oasis MontajTM: Tutorial and User Guide. Version, 6. 2005.
[41] A.M. Eldosouky, and S.A. Saada, *Arabian Journal of Geosciences*, *13*, (2020) 1-12.
[42] M.N. Nabighian, Geophysics, 37(3), (1972) 507-517.
[43] I.N. MacLeod, K. Jones, and T.F. Dai, *Exploration geophysics*, *24*(4), (1993) 679-688.
[44] A.B. Reid, J.M. Allsop, H. Granser, A.T. Millett, and I.W. Somerton, *Geophysics*, *55*(1), (1990) 80-91.
[45] J.B. Thurston, and R.S. Smith, *Geophysics*, *62*(3), (1997) 807-813.
[46] R.S. Smith, J.B. Thurston, T.F. Dai, and I.N. MacLeod, *Geophysical prospecting*, *46*(2), (1998) 141-151.
[47] A.M. Abudeif, M.A. Ali, and M.A. Mohammed, *Sohag Journal of Sciences*, *8*(3), (2023) 337-346.
[48] S. Elbarbary, M.A. Zaher, H. Mesbah, A. El-Shahat, and A. Embaby, *Renewable and Sustainable Energy Reviews*, *91*, (2018) 620-629.
[49] S.A. Saada, *Journal of Applied Geophysics*, *134*, (2016) 100-111.
[50] A.A. El-Khadragy, M.H. Saad and A. Azab, *Journal of Applied Science Research*, *61*(1), (2010) 22-27.
[51] M.A. Zaher, S. Elbarbary, S.A. Sultan, G., El-Qady, A. Ismail, and E.M. Takla, Geothermics, 75, (2018) 220-234.
[52] H. Saibi, S. Elbarbary, and M.A. Zaher, In The Geology of North Africa (501-515). Cham: Springer International Publishing. 2024.
[53] M., Rajaram, What's new in interpretation of magnetic data. *Geohorizons*, 50p, 2009.
[54] G.H. Halsey, and W.C. Gardner, Tectonic Analysis of Egypt using ERTS-1 Satellite Data: A Lecture Delivered at the General Petroleum Company of Egypt. 1975